*electronics*

MDPI

*Article*

# Efficiency, Cost, and Volume Comparison of SiC-Based and IGBT-Based Full-Scale Converter in PMSG Wind Turbine

**Jelena Loncarski [1,*], Hussain A. Hussain [2] and Alberto Bellini [1]**

[1] Department of Electrical, Electronic and Information Engineering "Guglielmo Marconi", University of Bologna, Via dell'Università 50, 47522 Cesena, Italy
[2] Department of Electrical Engineering, College of Engineering and Petroleum, Kuwait University, P.O. Box 5969, Safat, Kuwait City 13060, Kuwait
* Correspondence: jelena.loncarski2@unibo.it

**Abstract:** Power electronics, as an enabling technology in most renewable energy systems, is gaining attention as the penetration of renewable energy sources increases. Wide-bandgap power electronics are of particular interest due to their superior voltage blocking capabilities and fast switching speeds. They can viably be considered in the renewable energy sources, especially as the penetration of wind energy is expected to increase by a great extent in the upcoming years. In this paper, a comparison of Silicon Carbide-based and Silicon-based wind energy conversion systems has been performed, as it is crucial in understanding the benefits of adopting wide-bandgap-based solutions at a commercial level. For this analysis, a 2 MW permanent magnet synchronous generator-based wind conversion system with a bidirectional full-scale frequency converter comprised of two back-to-back inverters is considered. The efficiency, cost, and total volume of the passive components comparison have been conducted for Silicon- and Silicon Carbide-based converters. The comparison presented is a fair comparison, meaning that the converters are designed with modules of the same power ratings. Wind energy systems are compared both for the same switching frequency (low switching frequency suitable for IGBT modules) and also considering a Silicon Carbide-MOSFET-based converter working at high switching frequencies. The comparison is performed in PLECS simulation tool, using the PLECS libraries for different modules obtained from the manufacturers' experimental data. The results show the benefits of using the Silicon Carbide-based converter when it comes to volume reduction in the passive components and provide insights to what is missing in order to achieve overall system volume and cost savings.

**Keywords:** SiC devices; Si devices; wind energy converter; efficiency comparison; direct-driven PMSG wind turbine

check for updates

**Citation:** Loncarski, J.; Hussain, H.A.; Bellini, A. Efficiency, Cost, and Volume Comparison of SiC-Based and Igbt-Based Full-Scale Converter in PMSG Wind Turbine . *Electronics* **2023**, *12*, 385. https://doi.org/10.3390/electronics12020385

Academic Editor: Davide Astolfi

Received: 20 December 2022
Revised: 6 January 2023
Accepted: 9 January 2023
Published: 12 January 2023

**Copyright:** © 2023 by the authors. Licensee MDPI, Basel, Switzerland. This article is an open access article distributed under the terms and conditions of the Creative Commons Attribution (CC BY) license (https://creativecommons.org/licenses/by/4.0/).

## 1. Introduction

Global warming concerns and the depletion of fossil fuels have brought the need for alternative energy sources. Renewable Energy (RE) sources are playing a major role in green energy goals and can viably be utilized to overcome the gaps and supply green energy. The raising targets of REs in many countries are confirming this fact [1]. Recently, the record new additions of installed RE power capacities can be attributed to the low levelized cost of energy (LCOE) and technological innovation, particularly for solar photovoltaics and wind power.

Among the commercially available wind energy converters [2], the variable speed wind energy converter offers many benefits when compared to other commercially available types, such as the capability to have higher power density and minimize torque perturbations in the drive train. It is due to the capability of the wind turbine to operate at speeds that produce the greatest amount of power [3]. In the case of full-capacity converter wind energy systems, the power converter is of the same rating as the generator and, in this case, the generator is fully decoupled from the grid and able to operate in a full speed

range. This is not the case with doubly fed induction generator (DFIG)-based wind energy conversion systems, where only a fraction of the converted power passes through the converter (usually around 30%), resulting in reduced converter costs in comparison to the wind energy systems using full-capacity converters [4].

Nowadays, there is considerable interest in the application of the multiple-pole synchronous generators, either with permanent magnet excitation or with an electromagnet. They are driven by a wind-turbine rotor without a gearbox or with a low ratio gearbox [5]. The use of a synchronous generator leads to the requirement for a fully rated power electronic conversion system to decouple the generator from the network. A multi-pole permanent magnet synchronous generator (PMSG) with a full power back-to-back converter offers reduced losses and lower weight when compared to the externally excited SG [6].

Many technical solutions of wind turbine electrical systems are related to power electronics, owing to the possibility to control the wind turbine generator, improve dynamic and steady-state performances, and decouple the generator from the electrical grid. It is especially true in the case of PMSG-based wind farms, as they are being increasingly integrated to power grids. For this reason, the reliability of the PMSG system is becoming crucial and, in particular, the cost and the reliability of the power electronics system, as most of the power is processed by the power converter [7,8]. To reduce the maintenance cost, direct-driven wind turbines using low-speed PMSGs are a viable technology, as the costs for these turbines are reduced due to the elimination of the gearbox and brushes. However, a low-speed generator requires a larger diameter to accommodate the large number of poles on the perimeter, which is leading to increased generator and installation costs [9].

Regarding the power electronics interfacing renewable energy sources, significant improvements in Silicon (Si) power device technology have been produced in recent decades, causing this technology to be reliable and cost-effective. Newer power devices based on wide bandgap (WBG) materials, such as Silicon Carbide (SiC) and Gallium Nitride (GaN), are being developed in recent years. For renewable energy application, they can be seen as preferred devices as they offer several benefits when compared to their Si counterparts [10–12]. The most important ones are: lower losses, higher temperature, and high-frequency operation. Due to the lower losses, the net energy production can be increased and, thus, the cost of the converter itself can be potentially decreased. In addition, the use of SiC devices require a smaller cooling system and the output filter volume and weight can be reduced, causing, in this way, a direct impact on the system cost and decreasing the levelized cost of the energy (LCOE) of wind energy systems.

In order to understand the real benefits of SiC-based conversion systems, it is necessary to conduct a comparison with Si-based conversion systems. In the literature, there have been many recent works comparing SiC- and Si-based conversion systems for different kind of wind energy systems, as shown in Table 1. In [13], a 2 MW DFIG-based wind energy system has been considered and conclusions regarding the efficiency increase and volume reduction have been conducted. In [14], a PMSG-based 10 kW small-scale wind turbine is considered, where a performance benchmarking of Si-IGBTs- and SiC-MOSFETs-based inverters have been performed, pointing out the benefits in reduced filter volume, DC-link capacitor volume, and heatsink volume. In [15], a 2 MW PM generator-based wind generation system has been compared for the converters with Si IGBT, hybrid, and full SiC MOSFET devices in terms of efficiency and annual energy production. However, considering the converters with different power ratings, it is not clear which is the switching frequency of the simulated operating points. Another not so recent work [16] considered the 1.5 MW PMSG-based wind conversion system benchmarking for Si- and SiC-based converters in terms of their efficiencies. Furthermore, in this case, the system was sized differently for the IGBT and SiC devices, as the SiC devices were commercialized for lower currents, i.e., 50 A. Many devices and many converters needed to be connected in parallel. In a recently published paper [17], the 2 MW PMSG-based wind conversion system was considered and a fair comparison was introduced (in terms of device rating). A comparison

of the efficiency and volume was conducted, showing a higher efficiency for the SiC-based converter and the total volume reduction.

**Table 1.** Literature review.

| References | Generator | Same Device Ratings | Compared Variables |
|---|---|---|---|
| [13] | DFIG/2 MW | No | Efficiency and volume |
| [14] | PMSG/10 kW | No | Efficiency, cost, volume, and energy savings |
| [15] | PMSG/2 MW | No | Conduction characteristics, switching energy, efficiency, and annual energy production |
| [16] | PMSG/1.5 MW | No | Efficiency, losses, and volume |
| [17] | PMSG/2 MW | Yes | Efficiency and volume |

This work, however, is not showing the cost analysis, which is of the same importance as the efficiency and volume analysis in order to provide the full picture for decision making. In order to extend the analysis and fill the missing gap, this work is considering the same system, i.e., a 2 MW direct-driven PMSG wind turbine model with a bidirectional full-scale frequency converter comprising two back-to-back inverters but is also offering the overall system comparison including the efficiency, volume, and cost. The fair comparison considers the converters designed in the same way, with the half-bridge modules of the same ratings. The wind energy systems are compared for both the same switching frequency (i.e., considering low-switching frequency suitable for the IGBT module) and considering also the high switching frequencies for the SiC-MOSFET-based converter. The comparison is performed in the PLECS simulation tool, with PLECS libraries for different modules obtained from the manufacturers' experimental data.

## 2. Wind Turbine System and Modeling

### *2.1. Wind Turbine Model*

The extractable power from the wind is provided by [18]:

$$P = \frac{1}{2}\rho\pi R^2 v^3 c_p(\lambda, \beta) \tag{1}$$

where $\rho$ is the air density, $R$ is the turbine blade radius, $v$ is the wind speed, and $c_p$ is the power coefficient. The power coefficient $c_p$ is a function of the tip-speed-ratio $\lambda$ and the blade angle $\beta$. In the model, the power coefficient is implemented using a lookup table or approximated using equations. The variable speed control of the wind turbine allows for maximizing the power coefficient and thus the extracted power. The power coefficient can be approximated by [19]:

$$c_p(\lambda, \beta) = 0.22\left(\frac{120}{\lambda_i} - 0.4\beta - 5\right)e^{\frac{-12.5}{\lambda_i}} \tag{2}$$

$$\frac{1}{\lambda_i} = \frac{1}{\lambda + 0.08\beta} - \frac{0.035}{\beta^3 + 1} \tag{3}$$

The wind turbine system is composed of a 2 MW wind turbine, a permanent magnet synchronous generator rated at 690 V, a bidirectional full-scale frequency converter comprising two back-to-back converters, and an LCL filter, as shown in Figure 1. The dq electric model of the PMSG can be obtained using a Park transformation with an angle rotating in synchronization with the rotor electric angle $\theta_e$ [20]:

$$v_d = R_s i_d + \frac{d}{dt}L_d i_d - \omega_e L_q i_q \tag{4}$$

$$v_q = R_s i_q + \frac{d}{dt} L_q i_q + \omega_e L_d i_d + \omega_e \lambda_{pm} \tag{5}$$

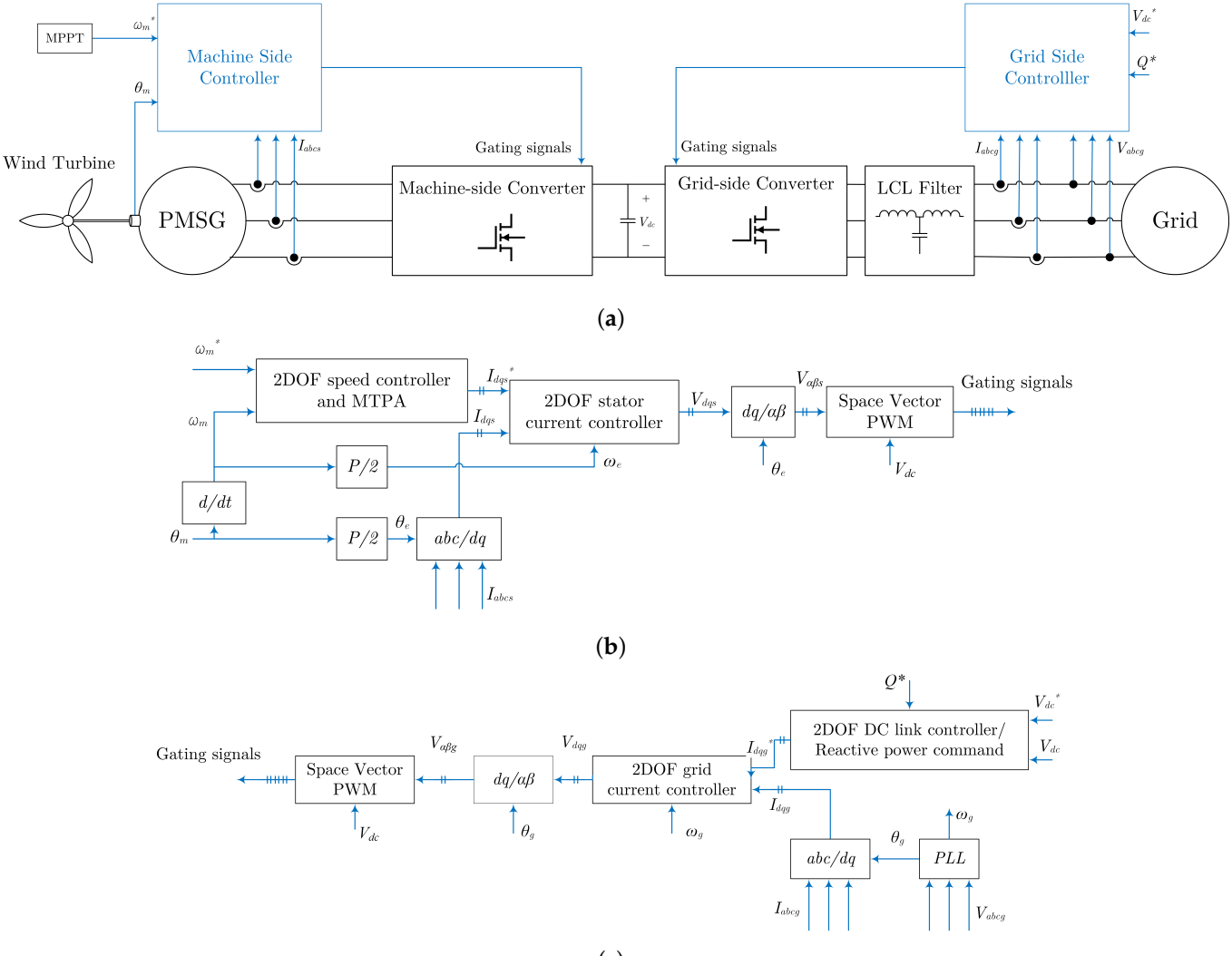


(**a**)

(**b**)

(**c**)

**Figure 1.** Block diagram of the wind turbine converter: (**a**) The overall system, (**b**) The control of the machine-side converter, and (**c**) The control of the grid-side converter.

The torque equation and the mechanical model are provided by [20]:

$$T_e = \frac{3}{2}\frac{P}{2}\left(\lambda_{pm} i_q + \left(L_d - L_q\right) i_d i_q\right) \tag{6}$$

$$J\frac{d\omega_m}{dt} + B\omega_m = T_e - T_m \tag{7}$$

$$\omega_e = \frac{P}{2}\omega_m \tag{8}$$

where $R_s$ is the stator resistance, $L_d$ is the stator direct-axis inductance, $L_q$ is the stator quadrature-axis inductance, $P$ is the pole number, $J$ is the total moment of inertia, $B$ is the friction coefficient, $\omega_e$ is the electrical frequency, $\omega_m$ is the mechanical frequency, $T_e$ is the electromagnetic torque, and $T_m$ is the turbine mechanical torque. The main generator and turbine parameters are listed in Table 2 [21].

**Table 2.** Generator and other parameters.

| **Generator Parameters** | |
|---|---|
| Rated power (MW) | 2 |
| Nominal voltage (V) | 690 |
| Rated speed (rpm) | 18 |
| Number of Poles | 60 |
| Stator resistance (mΩ) | 7 |
| Stator d-axis inductance (mH) | 0.8 |
| Stator q-axis inductance (mH) | 1.54 |
| **Turbine Parameters** | |
| Rotor diameter (m) | 82 |
| Hub height (m) | 78–108 |
| Cut-in wind speed (m/s) | 2.5 |
| Cut-out wind speed (m/s) | 28–34 |
| Rated wind speed (m/s) | 12 |
| **Other Parameters** | |
| DC-link voltage (V) | 1200 |
| Grid line-to-line voltage (V) | 690 |

The PMSG terminals are connected to a DC bus through four controlled rectifiers connected in parallel. Each controlled rectifier consists of a two-level AC/DC converter controlled for maximum wind power extraction, as shown in Figure 1. The PMSG is equipped with current sensors and a position sensor that is used to derive the shaft speed too. The measured currents are transformed into the dq rotating reference frame using Park transformation.

The machine-side converter is used to control the machine for maximum wind power extraction. A cascaded control structure is used to control the PMSG with an inner machine currents loop and an outer speed loop as shown in Figure 1b. The reference speed command $\omega_m^*$ is determined using the Maximum Power Point Tracking (MPPT) method. In the outer loop, a speed controller utilizes the reference speed command $\omega_m^*$ and the actual PMSG speed $\omega_m$ to generate the torque command. A maximum torque per ampere (2DOF speed controller and MTPA) block is used to generate the reference d-axis and q-axis $I_{dqs}^*$ machine current commands. In the inner loop, the current controller (2DOF stator current controller block) utilizes the reference current commands $I_{dqs}^*$ and the actual currents $I_{dqs}$ to generate the command voltages $V_{dqs}$. Finally, Inverse Park transformation and Space Vector Pulse Width Modulation (SVPWM) are used to generate the gate signals for the machine-side converter switches. In both the inner and outer loops, two-degrees-of-freedom (2DOF) PI controllers [22] are used to control the speed and currents of the machine.

On the other side, the DC bus is connected to the grid through four inverters connected in parallel and a three-phase LCL filter. Each inverter consists of a two-level DC/AC converter. The grid voltages and currents are measured using voltage and current sensors. Using the grid voltages, the grid angle $\theta_g$ and frequency $\omega_g$ are derived using a Phased Locked Loop (PLL) block. The grid angle $\theta_g$ is used to transform the voltages and currents into a dq reference frame rotating with the grid voltage vector. Another voltage sensor is used to measure the DC bus voltage $V_{dc}$.

The grid-side converter is used to control the DC bus voltage and the reactive power injected into the grid. Again, a cascaded control structure with an inner grid currents loop and an outer DC voltage loop is selected as shown in Figure 1c. In the outer loop, a DC link controller (2DOF DC link controller/Reactive power command block) utilizes the reference DC voltage command $V_{dc}^*$, the actual DC voltage $V_{dc}$, and the desired reactive power $Q^*$ to generate the reference d-axis and q-axis $I_{dqg}^*$ grid current commands. In the inner loop, two current controllers (2DOF grid current controller block) utilize the reference grid current commands $I_{dqg}^*$ and the actual grid currents $I_{dqg}$ to generate the command voltages $V_{dqg}$.

Next, the inverse Park transformation and SVPWM are used to generate the gate signals for the grid-side converter switches. Again, 2DOF PI controllers are used in the inner and outer loops.

### 2.2. Converter

A 2MW converter is required to provide full power conditioning for the generator output. The half-bridge modules of the same power ratings (1700 V, 650 A) have been chosen for this analysis, i.e., SiC-MOSFET module CAB650M17HM3 (Wolfspeed) [23] and Si-IGBT module FF650R17IE4P (Infineon) [24], as shown in Table 3. Three of these modules are connected to form a two-level 3-phase inverter. The current through the devices is split between diode and SiC-MOSFET/IGBT depending on the current polarity. In order to reach the current rating of the turbine (2200 $A_{rms}$), four of these back-to-back converters are connected in parallel.

**Table 3.** Module parameters.

| Parameters | SiC HB Module | IGBT HB Module |
|---|---|---|
| $V_{ds}$ | 1700 V | 1700 V |
| $I_{ds}/I_c$ (25 °C) | 916 A | 650 A |
| $I_{ds}/I_c$ | 694 A @ 90 °C | 650 A @ 125 °C |
| $R_{DS(on)}$ (175 °C) | 3.26 mΩ | N/A |
| $Q_g$ | 2988 nC @ −4/15 V | 7$\mu$C @ −15/15 V |
| $T_j$ | 175 °C | 175 °C |
| $R_{g\_on}$ (min) | 1.5 Ω | 1.8 Ω |
| $R_{g\_off}$ (min) | 1.5 Ω | 2.7 Ω |

### 2.3. Filter

An LCL-type filter was selected since it offers reduced size and increased attenuation compared to an L-type filter. The main disadvantage of the LCL filter is that it requires passive or active damping for stable operation, which may increase the complexity of the system. The LCL filter consists of an inverter-side inductor $L_i$, a grid-side inductor $L_g$, and a capacitor $C_f$ as shown in Figure 1. The LCL filter is designed as follows. First, the inverter-side inductor $L_i$ is designed based on the current ripple and the switching frequency as [25]:

$$L_i = \frac{2}{3}\frac{V_{dc}}{\Delta I_g f_{sw}}(1-m)m \tag{9}$$

where $\Delta I_g$ is the desired current ripple, $V_{dc}$ is the dc bus voltage, $f_{sw}$ is the switching frequency, and $m$ is the modulation index. Then the grid-side inductor $L_g$ is selected to as a ratio of $L_i$:

$$L_g = rL_i \tag{10}$$

where $r$ is the ratio that is selected to be 15%. Finally, the filter capacitor is selected based on the total harmonic distortion (THD) using:

$$C_f = \frac{1}{L_g(2\pi f_{sw})^2 \frac{THD}{k_i}} \tag{11}$$

where $k_i$ is the percentage ripple in the current $k_i = \Delta I_g / I_{g(peak)}$.

Table 4 summarizes the values of the filter parameters at 3 kHz and 30 kHz.

**Table 4.** LCL filter parameters for different switching frequencies.

| Paramerters | 3 kHz | 30 kHz |
|---|---|---|
| $L_i[\mu H]$ | 234.7 | 23.47 |
| $L_g[\mu H]$ | 35.2 | 3.52 |
| $C_f[\mu F]$ | 799.5 | 79.95 |

## 3. Losses and Volume Analysis

The complete wind conversion system has been built in a PLECS simulation tool, which is offering the possibility to the user to merge the thermal and electrical design and provide the cooling solutions.

### *3.1. Converter Losses*

The switching and conduction losses of the modules are inserted for each operating condition (forward current, blocking voltage, and junction temperature) in terms of 3D look-up tables. An example of such losses is shown in Figure 2, for SiC-MOSFET Figure 2a, and Si-IGBT module Figure 2b. In the figures, the depicted energy, $E_{base}$, is afterwords used to calculate the switching energy during the turn-on and turn-off processes in the case of different external on-gate resistances $R_{g\_on}$ and external off-gate resistances $R_{g\_off}$. In the case of the SiC-MOSFET module, the following equations have been used (provided in the PLECS library and obtained as the curve fitting of the losses provided in the datasheet in Figure 15 [23]):

$$E_{on} = E_{base}(-0.62834R_{g\_on}^2 + 16.4425R_{g\_on} + 30.1859)/53.4359 \quad (12)$$

$$E_{off} = E_{base}(0.38317R_{g\_off}^2 + 10.8655R_{g\_off} + 12.8655)/30.0259 \quad (13)$$

Instead, for the case of Si-IGBT module, the following equations have been used (provided in the PLECS library as the curve fitting of the losses provided in the datasheet [24] ($E_{on} = f(R_G), E_{off} = f(R_G)$):

$$E_{on} = E_{base}[-157.5114/(R_{g\_on}/1.8 + 15.8189) - 0.0810(R_{g\_on}/1.8) + 10.43581] \quad (14)$$

$$E_{off} = E_{base}[0.00028/(R_{g\_off}/2.7 + 14.3878) + 0.0403(R_{g\_off}/2.7) + 0.9593] \quad (15)$$

In further analysis, the minimum external gate resistances recommended by manufacturers have been applied (Table 3). The losses have been verified experimentally by the manufacturer in the standard double pulse-testing setup. A Cauer thermal network has been utilized for the thermal description of the modules.

After the loss description was added in PLECS and the thermal network was created for each converter, it was possible to select the appropriate heat sink. In this way, the respective converter losses together with the junction and heat sink temperature can be measured.

### *3.2. Volume Analysis*

In this section, both the heat sink and filter volumes are analyzed. When it comes to the heat sink volume, liquid cooling has been considered due to the low values of the thermal resistances. The heat sink volume analysis was based on the power loss of the two converters (with both SiC-MOSFET and Si-IGBT modules) for different switching frequencies and at a nominal wind speed of 12 m/s, considering an 80 °C heat sink temperature, and 25 °C and 55 °C of the ambient temperature. The minimum required gate resistances $R_{g\_on}$ and $R_{g\_off}$ were used, as they allow the lowest switching losses.

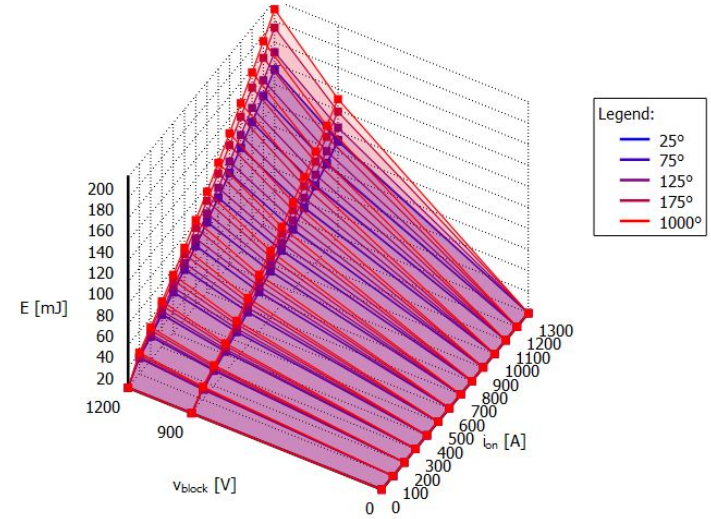


(**a**)

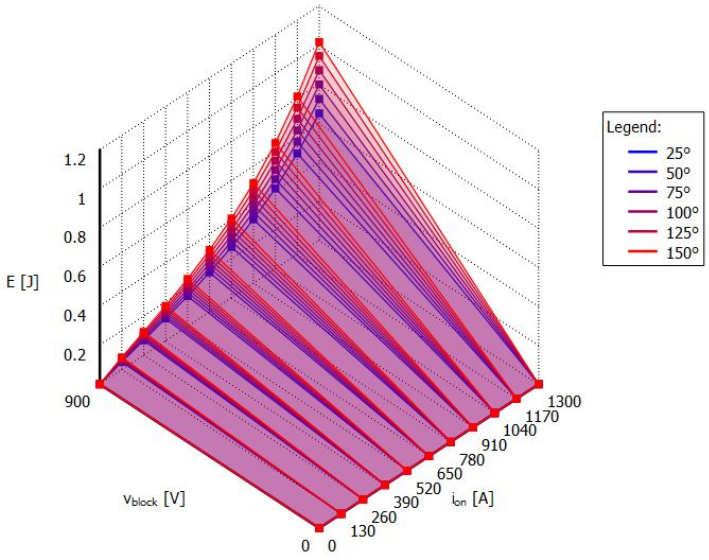


(**b**)

**Figure 2.** Example of module base-switching energies during the turn-on $E_{base}$ for different temperatures: (**a**) SiC-MOSFET, (**b**) Si-IGBT.

In order to evaluate the heat sink volume, it is necessary to calculate its thermal resistance:

$$r_h = \frac{T_h - T_a}{P_{tloss}} \tag{16}$$

where $T_h$ is the heat sink temperature, $T_a$ is the ambient temperature, and $P_{tloss}$ is the total converter loss. Once the $r_h$ is calculated, it is possible to obtain the heat sink volume based on the liquid cold plates cooling. Three different cold plates have been analysed from three different manufacturers [26–28], as shown in Figure 3, with the flow rate of 4 L/m. For the minimum volume [27], the curve fitting has been obtained:

$$vol_{heatsink} = 0.00036 {r_h}^{(-1.52)} \tag{17}$$

where $vol_{heatsink}$ is expressed in $dm^3$ and $r_h$ in °C/W. In this way, the volume for different thermal resistances can be obtained. The volume obtained with the fitting curve is including only the volume of the cold plates and not the volume of additional components (as it can be considered the same for the two conversion systems).

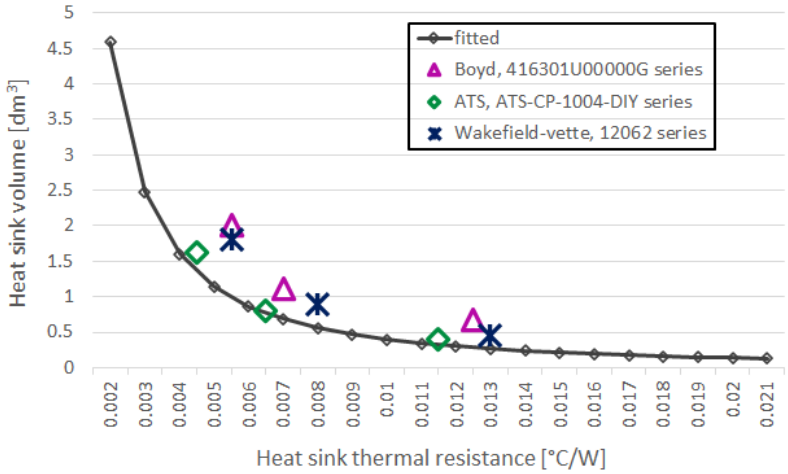


**Figure 3.** The volume of liquid cold plate heat sinks from different manufacturers.

The filter's inductors and capacitor volumes were calculated using [29]:

$$vol_L = k_L A_p^{3/4} \tag{18}$$

$$vol_C = k_c C_f V_{nom} \tag{19}$$

where $A_p$ is the area product defined as the product of the core window winding area and the cross-sectional area, $V_{nom}$ is the nominal voltage, and $k_L$ and $k_C$ are the inductor and capacitor coefficients, respectively.

## 4. Results and Discussion

In this section, the efficiency, volume, and cost comparisons have been performed considering two wind conversion systems (SiC-MOSFET- and Si-IGBT-based), including both the grid-side and machine-side converter. Figure 4 shows the efficiency of the two conversion systems in the case of different switching frequencies. In particular, two values for the external gate on and off resistances are considered for the SiC-MOSFET-based converter: the minimum ones required for a SiC-MOSFET-based converter ($R_{g\_on}$ = 1.5 Ω, $R_{g\_off}$ = 1.5 Ω) and the minimum ones required for a Si-IGBT-based converter ($R_{g\_on}$ = 1.8 Ω, $R_{g\_off}$ = 2.7 Ω). For the latter, the heat sink temperature of 60 °C is considered, while in other cases it was 80 °C. For the Si-IGBT-based conversion system, only one value of external on and off gate resistance has been considered, which is the minimum required ($R_{g\_on}$ = 1.8 Ω, $R_{g\_off}$ = 2.7 Ω). The nominal wind speed of 12 m/s was taken into account.

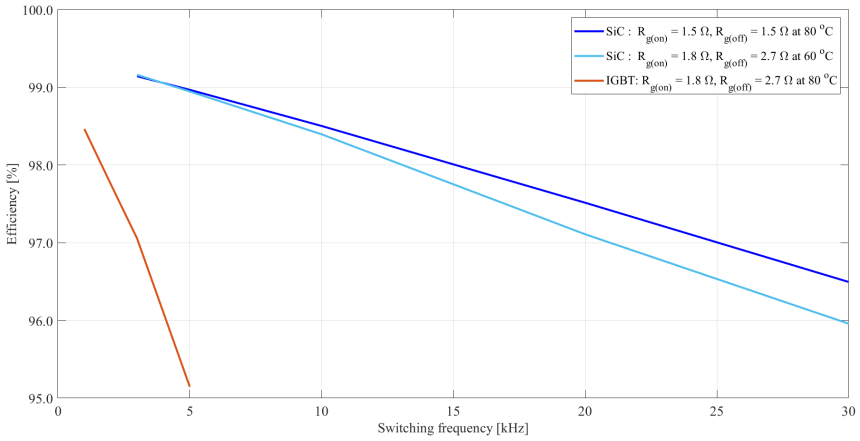


**Figure 4.** Efficiency for wind turbine converters at full power rating and different switching frequencies and external gate resistances.

The switching frequency ranges from 0 to 30 kHz for the SiC-MOSFET-based converter, while Si-IGBT-based converter ranges from 0 to 5 kHz. The reason behind this choice is that only the realistic conditions have been applied to both conversion systems. As for the low switching frequencies (3 and 5 kHz), the SiC-MOSFET-based converter shows higher efficiency, 2% higher in the case of a 3 kHz switching frequency and 4% higher in the case of a 5 kHz switching frequency. For the optimal switching frequency for both converters (30 kHz for SiC-MOSFET and 3 kHz for Si-IGBT converter) and minimum recommended external gate resistances, the efficiency is rather similar, lower 0.6% for a SiC-MOSFET -based converter.

When it comes to the volume analysis, the respective volumes of the passive components are shown in Figure 5. In particular, it shows: the grid-side and inverter-side inductor volumes, capacitor volume, and total filter volume (red trace) in Figure 5a and, in Figure 5b, the heat sink volumes of the SiC-MOSFET-based converter (red and light blue trace) and the heat sink volumes of the Si-IGBT-based converter (green and yellow trace) at 25 °C and 55 °C ambient temperature. When it comes to the filter volume, it is clear that the inverter-side inductor is the largest component in the filter (yellow trace in Figure 5a). The capacitor volume is negligible when compared to other volumes. The overall filter volume decreases as the switching frequency increases. This is not the case with the heat sink volume, which increases with the switching frequency. When considering the different ambient temperatures, i.e., 25 °C and 55 °C, the heat sink volume at 55 °C is 3.3 times higher than the one at 25 °C.

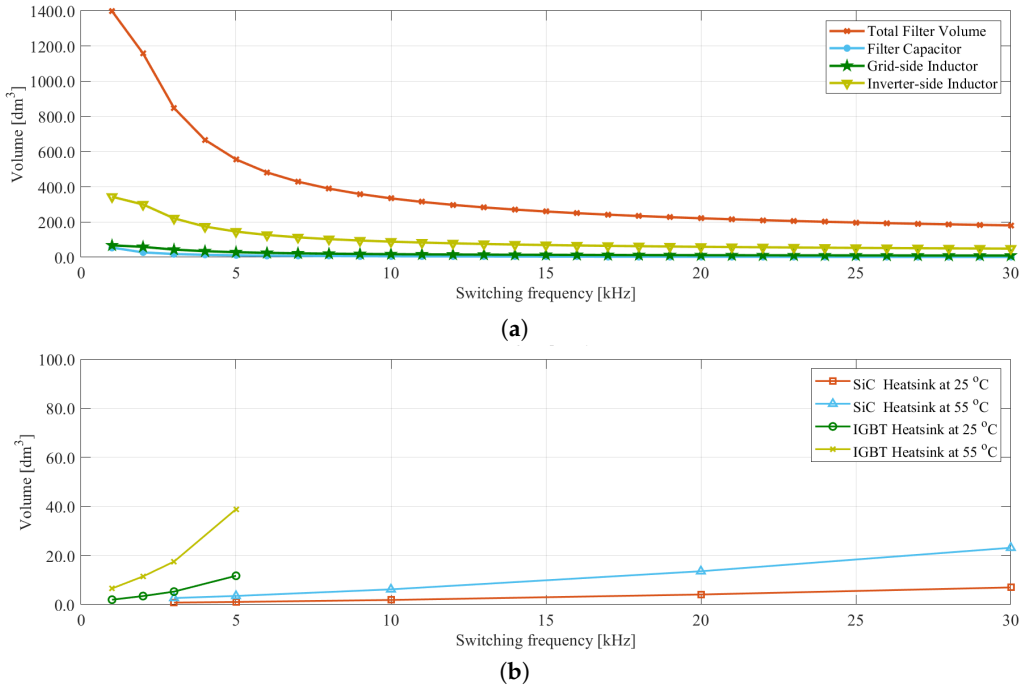


**Figure 5.** Different passive components volumes for different switching frequencies: (**a**) filter volume, (**b**) heat sink volume.

It can be noted that for the optimal switching frequencies (i.e., 30 kHz for SiC-MOSFET-based converter and 3 kHz for Si-IGBT-based converter), the heat sink volumes are rather similar, which is confirmed also by Figure 4, where the efficiencies for these two points are also similar.

Figure 6 shows an efficiency comparison for different wind speeds, considering 3 kHz and 30 kHz switching frequencies for the SiC-MOSFET-based converter (blue and light blue traces) and 3 kHz for the Si-IGBT-based converter (red trace) (Figure 6a), together with a total volume comparison in the case of the nominal wind speed of 12 m/s (in dm$^3$, including the filter and heat sink volume) and a cost comparison of the converter, filter,

and heat sink (in euros) (Figure 6b). The following parameters have been considered for the comparison: the minimum required on and off external gate resistances for both the conversion systems as in Table 3 and the heat sink temperature of 80 °C.

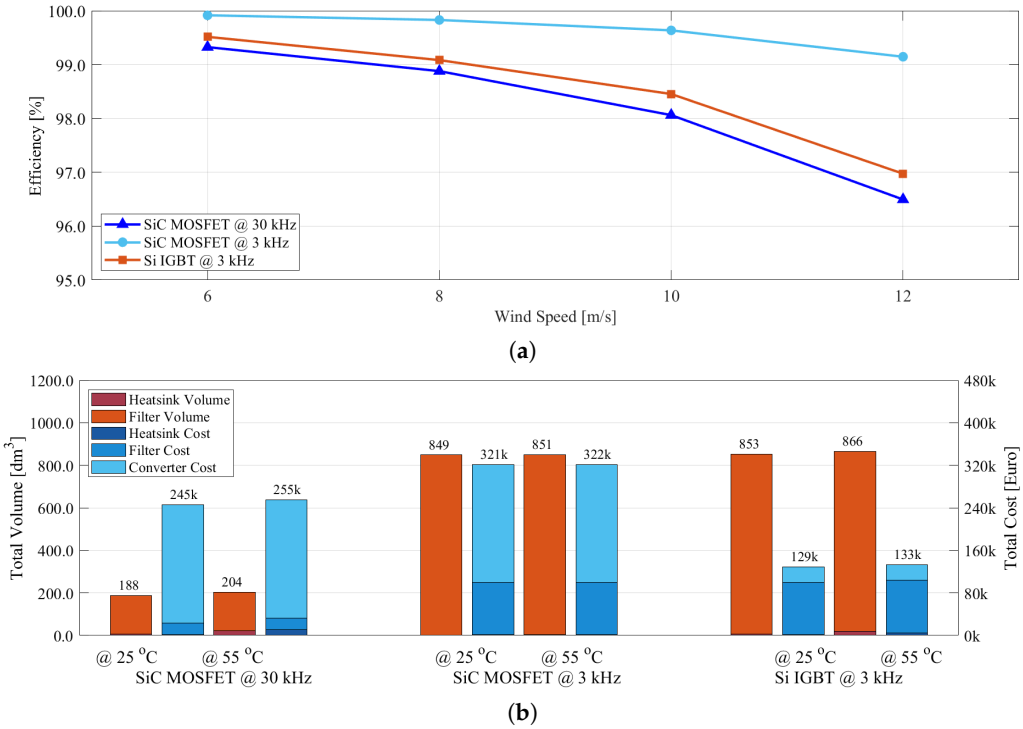


**Figure 6.** Comparison of SiC-MOSFET- and Si-IGBT-based converters for different wind speeds and 30 kHz and 3 kHz switching frequencies: (**a**) efficiency, (**b**) cost and volume.

As for the cost analysis, the average prices for specific volumes from main distributors have been taken into account, which have then been fitted in order to obtain the volumes resulted in the analysis. For the heat sink, the average cost of the selected minimum volume liquid cooling solution from [27] has been taken into account:

$$cost_{heatsink} = 96.27928 + 29.62853 * e^{(1.111726 vol_{heatsink})} \quad (20)$$

As for the filter, the information on the different filters' costs available in [30] has been used to obtain the curve fitting:

$$cost_{filter} = 114.5 * vol_{filter} + 857.2 \quad (21)$$

where the prices are expressed in euros and the volumes in $dm^3$.

For the 3 kHz case in Figure 6a, the SiC-MOSFET-based converter shows higher efficiency for all the wind speeds considered, with the highest difference of around 2% at maximum wind speed. When considering the most optimal switching frequencies for both converters, the difference is rather restrained, having the SiC-MOSFET-based converter at a slightly lower efficiency. The similar result is obtained also in other analyses that are dealing with the SiC-MOSFET and Si-IGBT converter comparisons [13,16].

As for the volume, the heat sink volume is negligible when compared to filter volume in all cases. The SiC-MOSFET-based converter with a 30 kHz switching frequency has the lowest total volume, 4.52 times lower (4.17 times in the case of 55 °C ambient temperature) when compared to a SiC-MOSFET-based converter at 3 kHz and 4.54 times lower (4.25 in the case of 55 °C ambient temperature) when compared to Si-IGBT-based converter at 3 kHz. When looking to the different costs, again, the heat sink cost is almost negligible when compared to the cost of the filter and converter. The highest cost in the SiC-MOSFET-

based converter is the converter cost, which is 7.5 times higher when compared to the Si-IGBT-based converter. The filter cost, instead, for the SiC-MOSFET-based converter at 30 kHz is 4.54 times lower than the one at 3 kHz.

When looking to the SiC-MOSFET-based converter at 3 kHz, the only benefit can be seen in the efficiency. This case collects the disadvantages of the other two cases for the nominal wind speed (Figure 6b); it has a high volume due to the high filter volume and the highest cost mainly due to the high converter cost, but it also has a high filter cost as the switching frequency is low. It is interesting to notice the similar volumes and costs for the 25 °C and 55 °C ambient temperatures, which is due to there being very little change in the heat sink volume as the efficiency is rather high and, consequently, the thermal resistance is higher, in this case causing the difference in the volume to be lower, as in Figure 3.

Leaving aside the SiC-MOSFET-based converter with the 3 kHz switching frequency and looking only at two converters in their optimal working conditions (i.e., 3 kHz for Si-IGBT-based converter and 30 kHz for the SiC-MOSFET-based converter), it can be noted that for the similar converter efficiency at nominal wind speed (12 m/s), the SiC-MOSFET-based converter has a 4.54 times lower total volume filter cost when compared to the Si-IGBT-based converter, while its total cost (converter, filter, and heat sink) is about 2 times higher, mainly due to the high module cost.

In order to simplify the comparison, the cost function has been defined, based on the weighted parameters obtained by using the Analytic Hierarchy Approach (AHP) [31]. Namely, different priorities have been defined for the efficiency, volume, and cost, i.e., equal, moderate, and moderate, respectively. The reason behind this choice is to provide more importance to the cost and volume, as the the change in the efficiency is much lower than the change in the volume and cost. The calculated weighted constants are provided in Table 5.

After the weighted constants have been calculated, the efficiency, volume, and cost have been normalized with the maximum base values resulting from the simulation, i.e., 0.9914 for the efficiency, 853.42 for the volume, and 321,463.7 for the cost. The following cost function has been applied to the normalized values:

$$f_c = K_1/e_n + K_2 v_n + K_3 c_n \tag{22}$$

**Table 5.** AHP and cost function.

| **Weighted Parameters** | | | |
|---|---|---|---|
| Efficiency ($K_1$) | 0.143 | | |
| Volume ($K_2$) | 0.429 | | |
| Cost ($K_3$) | 0.429 | | |
| **Normalized efficiency, volume, and cost** | | | |
| | Efficiency ($e_n$) | Volume ($v_n$) | Cost ($c_n$) |
| SiC-MOSFET at 30 kHz | 0.973 | 0.22 | 0.763 |
| SiC-MOSFET at 3 kHz | 1 | 0.994 | 1 |
| Si-IGBT at 3 kHz | 0.979 | 1 | 0.401 |
| **Cost function results** | | | |
| SiC-MOSFET at 30 kHz | 0.568 | | |
| SiC-MOSFET at 3 kHz | 0.998 | | |
| Si-IGBT at 3 kHz | 0.747 | | |

The results of the cost function ($f_c$) are shown in Table 5. The SiC-MOSFET at 30 kHz has the best result (the minimum value) regardless of the high total cost (Figure 6b). The SiC-MOSFET at 3 kHz has the worst result, as the priority provided for the efficiency was less than the one for the cost and volume. The Si-IGBT converter has better results

than the one of the SiC-MOSFET-based inverter at 3 kHz, since for the similar total volume it has 2.5 times lower cost.

## 5. Conclusions

A 2 MW PMSG-based direct-driven wind conversion system was considered for this analysis and an efficiency, volume, and cost comparison for Si- and SiC-based converters was conducted. The simulations with the realistic thermal models of the modules have lead to the conclusion that the application of a SiC-based converter in the wind generation system will provide a similar efficiency to one of the Si-based converters, but will provide a reduction in the system's size. In particular, the reduction of 4.54 times (4.25 times in the case of 55 °C ambient temperature) in the total volume necessary for the passive components was observed, while the price increase was with a factor of 2. With the price reduction in SiC-MOSFET modules, the benefits of this system will be more marked, as the filter cost is much lower in this case. So, in order to have overall system cost and volume savings with the SiC-MOSFET-based conversion system, the price of the SiC devices should be substantially lower, at least 2 times in order to have an equal cost to the Si-based system. Moreover, the cost function applied to the efficiency, volume, and cost with different weights (less for the efficiency and equal to the cost and volume) has shown that the SiC-MOSFET-based converter at 30 kHz has the best value, regardless of its higher cost, when compared to a Si-IGBT converter, as the benefits in the volume reduction were superior.

**Author Contributions:** Conceptualization, J.L. and H.A.H.; methodology, J.L. and H.A.H.; software, J.L. and H.A.H.; validation, J.L. and H.A.H.; formal analysis, J.L., H.A.H. and A.B.; investigation, J.L. and H.A.H.; resources, J.L., H.A.H. and A.B.; data curation, J.L. and H.A.H.; writing—original draft preparation, J.L., H.A.H. and A.B.; writing—review and editing, J.L., H.A.H. and A.B. All authors have read and agreed to the published version of the manuscript.

**Funding:** This research received no external funding.

**Conflicts of Interest:** The authors declare no conflict of interest.

## References

1. Gielen, D.; Boshell, F.; Saygin, D.; Bazilian, M.D.; Wagner, N.; Gorini, R. The role of renewable energy in the global energy transformation. *Energy Strategy Rev.* **2019**, *24*, 38–50. [CrossRef]
2. Yaramasu, V.; Wu, B.; Sen, P.C.; Kouro, S.; Narimani, M. High-power wind energy conversion systems: State-of-the-art and emerging technologies. *Proc. IEEE* **2015**, *5*, 740–788. [CrossRef]
3. Zinger, D.S.; Muljadi, E. Annualized wind energy improvement using variable speeds. *IEEE Trans. Ind. Appl.* **1997**, *33*, 1444–1447. [CrossRef]
4. Blaabjerg, F.; Chen, Z. *Power Electronics for Modern Wind Turbines Turbines*; Morgan & Claypool Publishers: San Rafael, CA, USA, 2006.
5. Chen, Z.; Guerrero, J.M.; Blaabjerg, F. A Review of the State of the Art of Power Electronics for Wind Turbines. *IEEE Trans. Power Electron.* **2009**, *24*, 1859–1875. [CrossRef]
6. Blaabjerg, F.; Liserre, M.; Ma, K. Power electronics converters for wind turbine systems. *IEEE Trans. Ind. Appl.* **2012**, *48*, 708–719. [CrossRef]
7. Wang, H.; Ma, K.; Blaabjerg, F. Design for reliability of power electronic systems. In Proceedings of the IECON 2012—38th Annual Conference on IEEE Industrial Electronics Society, Montreal, QC, Canada, 25–28 October 2012; pp. 33–44.
8. Ye, S.; Zhou, D.; Yao, X.; Blaabjerg, F. Component-Level Reliability Assessment of a Direct-Drive PMSG Wind Power Converter Considering Two Terms of Thermal Cycles and the Parameter Sensitivity Analysis. *IEEE Trans. Power Electron.* **2021**, *36*, 10037–10050. [CrossRef]
9. Wu, B.; Lang, Y.; Kouro, S. *Power Conversion and Control of Wind Energy Systems*; John Wiley & Sons: Hoboken, NJ, USA, 2011.
10. Huang, A.Q. Power Semiconductor Devices for Smart Grid and Renewable Energy Systems. *Proc. IEEE* **2017**, *105*, 2019–2047. [CrossRef]
11. Zhang, H.; Tolbert, L.M. SiC's potential impact on the design of wind generation system. In Proceedings of the 2008 34th Annual Conference of IEEE Industrial Electronics, Orlando, FL, USA, 10–13 November 2008; pp. 2231–2235.
12. Hussein, A.; Castellazzi, A. Comprehensive design optimization of a wind power converter using SiC technology. In Proceedings of the 2018 International Conference on Smart Grid (icSmartGrid), Nagasaki, Japan, 4–6 December 2018; pp. 34–38.

13. Arrizabalaga, A.; Idarreta, A.; Mazuela, M.; Aizpuru, I.; Iraola, U.; Rodriguez, J.L.; Labiano, D.; Alişar, I. Impact of silicon carbide devices in 2 MW DFIG based wind energy system. In Proceedings of the 2020 22nd European Conference on Power Electronics and Applications (EPE'20 ECCE Europe), Lyon, France, 7–11 September 2020; pp. 1–10.
14. Hussein, A.; Castellazzi, A.; Wheeler, P.; Klumpner, C. Performance benchmark of Si IGBTs vs. SiC MOSFETs in small-scale wind energy conversion systems. In Proceedings of the 2016 IEEE International Power Electronics and Motion Control Conference (PEMC), Varna, Bulgaria, 25–28 September 2016; pp. 963–968.
15. Arrizabalaga, A.; Mazuela, M.; Idarreta, A.; Iraola, U.; Aizpuru, I.; Rodriguez, J.L.; Andueza, D.L.; Alişar, I. Integration of Silicon Carbide devices to increase the AEP (Annual Energy Production) in a PM based wind generation system. In Proceedings of the 2020 IEEE 11th International Symposium on Power Electronics for Distributed Generation Systems (PEDG), Dubrovnik, Croatia, 28 September–1 October 2020; pp. 482–486.
16. Zhang, H.; Tolbert, L.M. Efficiency Impact of Silicon Carbide Power Electronics for Modern Wind Turbine Full Scale Frequency Converter. *IEEE Trans. Ind. Electron.* **2011**, *58*, 21–28. [CrossRef]
17. Loncarski, J.; Hussain, H.A.; Bellini, A. High-power SiC Module in Wind Turbine Full Scale Frequency Converter: Efficiency Comparison with IGBT-based Converter. In Proceedings of the 2022 Second International Conference on Sustainable Mobility Applications, Renewables and Technology (SMART), Cassino, Italy, 23–25 November 2022; pp. 1–7.
18. Ackermann, T. *Wind Power in Power Systems*, 2nd ed.; John Wiley & Sons: Hoboken, NJ, USA, 2012.
19. Dai, J.; Liu, D.; Wen, L.; Long, X. Research on power coefficient of wind turbines based on SCADA data. *Renew. Energy* **2016**, *86*, 206–215. [CrossRef]
20. Lipo, T.A. *Analysis of Synchronous Machines*, 2nd ed.; CRC Press: Boca Raton, FL, USA, 2012.
21. VI-Technical Description E-82-Rev003ger-eng.doc. 2005. Available online: https://archives.bape.gouv.qc.ca/sections/mandats/eole-mrc-erable/documents/PR1_ann-1.pdf (accessed on 3 January 2023).
22. Hussain, H.A. Tuning and Performance Evaluation of 2DOF PI Current Controllers for PMSM Drives. *IEEE Trans. Transp. Electrif.* **2021**, *7*, 1401–1414. [CrossRef]
23. CAB650M17HM3 Product Information. 2022. Available online: https://assets.wolfspeed.com/uploads/dlm_uploads/2022/02/CAB650M17HM3.pdf (accessed on 11 October 2022).
24. FF650R17IE4P Product Information. 2022. Available online: https://www.infineon.com/dgdl/Infineon-FF650R17IE4P-DS-v03+00-EN.pdf?fileId=5546d46253e9fadc0153efeab1493c89 (accessed on 13 October 2022).
25. Reznik, A.; Simões, M.G.; Al-Durra, A.; Muyeen, S.M. *LCL* Filter Design and Performance Analysis for Grid-Interconnected Systems. *IEEE Trans. Ind. Appl.* **2014**, *50*, 1225–1232. [CrossRef]
26. Liquid Cooling Product Information (Boyd). Available online: https://info.boydcorp.com/hubfs/Thermal/Liquid-Cooling/Boyd-Hi-Contact-6-Pass-Datasheet.pdf (accessed on 3 January 2023).
27. Liquid Cooling Product Information (ATS). Available online: https://www.qats.com/Products/Liquid-Cooling/Cold-Plates/ATS-CP-1004-DIY (accessed on 3 January 2023).
28. Liquid Cooling Product Information (Wakefield-Vette). Available online: https://wakefieldthermal.com/content/data_sheets/Standard%20Liquid%20Cold%20Plates.pdf (accessed on 3 January 2023).
29. Gurpinar, E.; Castellazzi, A. Single-Phase T-Type Inverter Performance Benchmark Using Si IGBTs, SiC MOSFETs, and GaN HEMTs. *IEEE Trans. Power Electron.* **2016**, *31*, 7148–7160. [CrossRef]
30. Filter Product Information. Available online: https://www.mtecorp.com/ (accessed on 3 January 2023).
31. Ford, R.; Coulston, C. *Design for Electrical and Computer Engineers: Theory, Concepts, and Practice*; McGraw-Hill Education: New York, NY, USA, 2007.


**Disclaimer/Publisher's Note:** The statements, opinions and data contained in all publications are solely those of the individual author(s) and contributor(s) and not of MDPI and/or the editor(s). MDPI and/or the editor(s) disclaim responsibility for any injury to people or property resulting from any ideas, methods, instructions or products referred to in the content.